Fatigue and Corrosion Fatigue Properties of Mg–Zn–Zr–Nd Alloys in Glucose-Containing Simulated Body Fluids

Xue Han[1] · Dan Zhang[2] · Song Zhang[1] · Mohammed R. I. Abueida[2] · Lili Tan[3] · Xiaopeng Lu[4] · Qiang Wang[2] · Huanye Liu[2]

Abstract

Medical bone implant magnesium (Mg) alloys are subjected to both corrosive environments and complex loads in the human body. The increasing number of hyperglycemic and diabetic patients in recent years has brought new challenges to the fatigue performance of Mg alloys. Therefore, it is significant to study the corrosion fatigue (CF) behavior of medical Mg alloys in glucose-containing simulated body fluids for their clinical applications. Herein, the corrosion and fatigue properties of extruded Mg-Zn-Zr-Nd alloy in Hank's balanced salt solution (HBSS) containing different concentrations (1 g/L and 3 g/L) of glucose were investigated. The average grain size of the alloy is about 5 μm, which provides excellent overall mechanical properties. The conditional fatigue strength of the alloy was 127 MPa in air and 88 MPa and 70 MPa in HBSS containing 1 g/L glucose and 3 g/L glucose, respectively. Fatigue crack initiation points for alloys in air are oxide inclusions and in solution are corrosion pits. The corrosion rate of the alloy is high at the beginning, and decreases as the surface corrosion product layer thickens with the increase of immersion time. The corrosion products of the alloy are mainly $Mg(OH)_2$, MgO and a small amount of Ca-P compounds. The electrochemical results indicated that the corrosion rate of the alloys gradually decreased with increasing immersion time, but the corrosion tendency of the alloy was greater in HBSS containing 3 g/L glucose. On the one hand, glucose accelerates the corrosion process by adsorbing large amounts of aggressive Cl^- ions. On the other hand, glucose will be oxidized to form gluconic acid, and then reacts with $Mg(OH)_2$ and MgO to form Mg gluconate, which destroys the corrosion product film and leads to the aggravation of corrosion and the accumulation of fatigue damage.

Keywords Mg alloys · Corrosion fatigue · Glucose · Gluconic acid · Corrosion product

✉ Song Zhang
songzhang_sy@163.com

✉ Huanye Liu
dentist_ye@163.com

1 School of Materials Science and Engineering, Shenyang University of Technology, Shenyang 110870, China

2 School and Hospital of Stomatology, China Medical University, Shenyang 110001, China

3 Shi-Changxu Innovation Center for Advanced Materials, Institute of Metal Research, Chinese Academy of Sciences, Shenyang 110016, China

4 Shenyang National Laboratory for Materials Science, Northeastern University, Shenyang 110819, China

1 Introduction

As a biodegradable medical metal material, magnesium (Mg) and its alloys have the advantages of low density, high specific strength, suitable elastic modulus, good biocompatibility and excellent biomechanical compatibility [1–3]. This leads to a wide range of clinical applications in areas such as orthopedic repair and cardiovascular stents [4–6]. Compared to traditional medical implant metals (such as stainless steel, titanium, etc.), Mg alloy has the advantage of being completely degradable in the body, avoiding secondary surgeries that can cause harm to the patient [7–9]. Moreover, the degradation products of Mg alloys are non-toxic, and the excess Mg^{2+} ions after implant dissolution can be excreted from the body with body fluids through human metabolism [10–12].

On the one hand, nevertheless, Mg and its alloys are susceptible to hydrogen depolarization corrosion in physiological environments due to the standard electrode

potential of Mg being as low as -2.37 V, lower than that of the standard hydrogen electrode. This is especially true when aggressive Cl^- ions are present in bodily fluids [13–15]. This is one of the reasons why implants fail in advance before the trauma heals. On the other hand, Mg-based implants are subjected to complex stress effects after implantation into the human body. Human activities, such as walking, running, jumping, will subject the Mg-based metal materials used as human implants to cyclic loads [16, 17]. The interaction of the corrosive environment and cyclic loading carried by the body fluid itself will subject the Mg-based metal material to corrosion fatigue (CF), and this failure phenomenon under the combined effect of stress and corrosive environment will further accelerate the premature damage of the implant [18, 19]. This effect has greatly limited the widespread clinical application and development of Mg and its alloys.

It is well known that the exploration of CF properties of medical Mg alloys is inevitably inseparable from a variety of simulated physiological environments. A lot of previous work has been done to explore the effect of simulated body fluids containing inorganic salts on the corrosion of Mg alloys [11, 20–22]. However, it cannot be ignored that human body fluids contain not only inorganic ions but also various organic molecules and compounds, and their influence on the corrosion behavior of Mg alloys is also crucial. For example, Witte et al. [23] have demonstrated that the differences in the degradation of Mg and its alloys in vitro and in vivo are partly due to the influence of organic molecules.

Glucose is an important organic compound in the human body. It is one of the basic sources of energy, and it is important for the maintenance of human life and health. In recent years, unhealthy lifestyles and an ageing population have led to a dramatic increase in the number of people with hyperglycemia and diabetes [24]. Therefore, an unfavorable implant environment is more likely to lead to premature failure of Mg implants when they are at higher levels of glucose concentration [25]. The ability of Mg alloys to meet service requirements in hyperglycemic or diabetic patients is mainly dependent on their CF performance in environments containing body fluids with high glucose concentrations. A few studies have investigated the effect of glucose on the corrosion behavior of Mg and its alloys [26–28]. Zeng et al. [24] showed that glucose accelerated the corrosion of pure Mg in saline while inhibiting the corrosion of pure Mg in Hank's simulated body fluids. Li et al. [29] found that glucose concentration of 1 g L^{-1} inhibited the corrosion of AZ31 alloy in saline. However, when the concentration reached the level of diabetic patients, the degradation rate of AZ31 alloy was significantly accelerated. There are also findings demonstrated that high concentrations of glucose accelerated the corrosion of Mg–1.35Ca alloys in salt solution due to the massive adsorption of surface chloride ions [30].

Therefore, the dynamic CF behavior of Mg alloys in relation to glucose levels in physiological conditions needs to be further investigated. According to our earlier research, the hot-extruded Mg–2Zn–0.5Zr–0.5Nd alloy exhibits moderate biodegradability and good mechanical qualities [31–33]. But, the fatigue and CF behavior of the alloy in simulated body fluids containing organic matter (glucose) needs to be clarified. In the present study, the fatigue and corrosion fatigue behavior of Mg–2Zn–0.5Zr–0.5Nd alloy in HBSS containing different concentrations of glucose was investigated. To simulate normal and high glucose levels, the glucose concentration was set at 1 g/L and 3 g/L, respectively [34]. The aim of this study is to investigate the mechanism of glucose effect on CF of Mg alloys in a simulated physiological environment. The significance of this work is that it can provide theoretical guidance for the application of biomedical Mg alloy as a bone repair and implantation in patients with hyperglycemia or diabetes.

2 Material and Methods

2.1 Material and Characterization

Our team prepared the extruded Mg–2Zn–0.5Zr–0.5Nd alloy used in this study in a previous study [35]. The alloy matrix was cut into cylinders 10 mm in diameter and 5 mm in height for metallographic observation. The samples were sanded and polished with sandpaper, washed with anhydrous ethanol and blown dry. The samples were then etched in the picric acid solution for 10–15 s, removed, washed with anhydrous ethanol and blown dry. The microstructure of the samples was observed using a scanning electron microscope (Gemini SEM 460). The physical phase analysis of the alloy was performed using an X-ray diffractometer (XRD, Shimadzu 7000). A Cu$K\alpha$ target with a voltage of 30 kV and a current of 15 mA was equipped to the XRD, which was scanning at a speed of 4°/min from 20° to 100°.

2.2 Static Mechanical Properties Test

An Instron 5982 electronic universal testing equipment with a tensile speed of 1.0 mm/min was used to conduct static tensile testing. The test was repeated three times to avoid serendipity.

2.3 Fatigue and Corrosion Fatigue Test

Fatigue and CF tests were conducted using a computer-controlled electromagnetic dynamic mechanical testing machine with a tensile-compressive cycle, a stress ratio of $R = -1$ and a sinusoidal waveform ($R = -1$ stands for tension–compression fully reversed). Figure 1a shows the equipment for fatigue
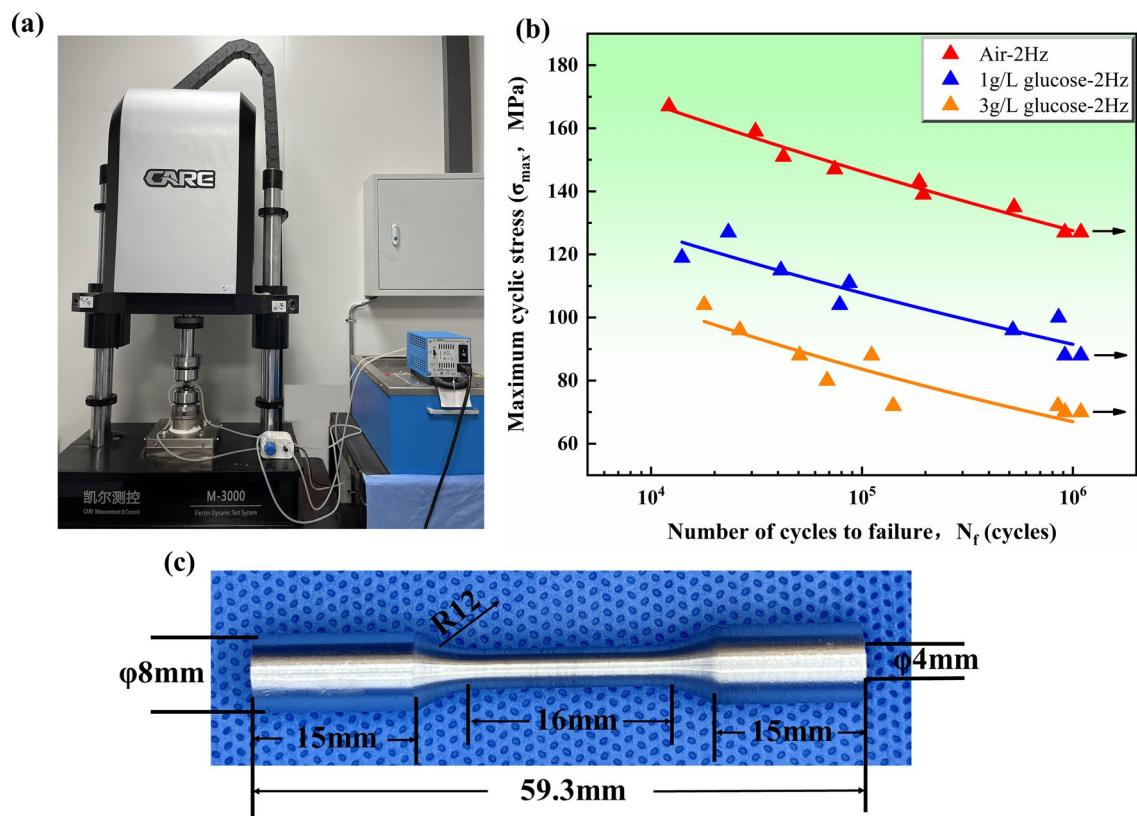
Fig. 1 Equipment diagram of fatigue test **a**, stress-life (S–N) curves of extruded Mg–2Zn–0.5Zr–0.5Nd alloy in air and HBSS containing different concentrations of glucose **b**, diagram of fatigue sample **c**

testing, model CARE Measurement and Control M-3000. An in-house dynamic liquid circulation system is used in the CF test to simulate the body's circulating environment. The solution was continually pumped through the corrosion chamber by a peristaltic pump, which controlled the flow rate to 120 mL/min [36]. The solution for the CF is HBSS; the composition shown in Table 1, and the temperature during the test is always maintained at 37 ± 1 °C. The specifications of the fatigue specimens tested in air and simulated body fluids are shown in Fig. 1c. The loading frequencies in this experiment were set to $f = 2$ Hz. The fatigue test is continued until the specimen fails or until the specimen reaches 10^6 cycles without failure. The CF failure samples were cleaned and blown dry with acetone and anhydrous ethanol, and then put into a 200 g/L CrO_3 chromic acid solution and 10 g/L $AgNO_3$ mixed with shaking to clean the corrosion products. The fracture morphology of the samples was observed and assessed using SEM and energy disperse spectroscopy (EDS).

2.4 Electrochemical Test

The corrosion behavior of Mg–2Zn–0.5Zr–0.5Nd alloys in HBSS containing different concentrations of glucose was investigated by electrochemical tests including open-circuit potential (OCP), electrochemical impedance spectra (EIS) and potentiodynamic polarization (PDP) using Gamry Reference 600 electrochemical workstation. The alloy was used as the working electrode, platinum sheet as the counter electrode and saturated calomel electrode as the reference electrode, respectively. Firstly, the specimen was ground to 3000 marks with sandpaper and then the wire was connected to one end of the specimen with a welder, then the specimen was sealed with epoxy resin to expose only the working electrode, and finally ultrasonically cleaned with alcohol and acetone. All tests were carried out in HBSS at a guaranteed temperature of 37 °C using a thermostatic water bath. A 30-min OCP test was performed prior to testing to ensure that the specimen surface

Table 1 Formulation of Hank's balanced salt solution (g/L)

Components	NaCl	CaCl$_2$	KCl	MgCl$_2$·6H$_2$O	MgSO$_4$·7H$_2$O	Na$_2$HPO$_4$·12H$_2$O	KH$_2$PO$_4$	NaHCO$_3$	C$_6$H$_6$O$_6$
Concentration	8.00	0.14	0.40	0.10	0.10	0.12	0.06	0.35	1.00

reached steady state. The EIS was measured at frequencies from 10^5 to 10^{-2} Hz with a 5 mV sinusoidal perturbing signal. The PDP test scans from -0.25 V below the OCP to 0.35 V above at a scan rate of 0.5 mV/s. The impedance data obtained were fitted with ZSimpWin software.

2.5 Immersion Test

The samples for the immersion test were cut into 10 mm diameter by 2 mm thick discs, which were then embedded in epoxy resin so that only the bottom surface was visible. The samples were then sandpapered, cleaned with anhydrous ethanol and blown dry. The HBSS used for the immersion test is shown in Table 1. The immersion ratio was 20 mL/cm^2, and the temperature was 37 ± 1 °C [37, 38]. The treated samples were immersed in beakers containing HBSS for 14 days, during which time the solution was changed every 24 h and the pH of the solution was measured. Besides, the corrosion rate of the alloys was tested by weight loss. Before measuring the weight of the exposed specimens in the weight loss test, their surfaces were treated with chromate solution (200 g/L CrO$_3$+10 g/L AgNO$_3$) for 5 min to remove the degradation products. Subsequently, specimens were ultrasonically cleaned in acetone for 1 min and dried at 37 °C for 24 h. At the end of the immersion test, the sample used to observation the corrosion product cross-section layer was cut longitudinally along the diameter. The corrosion products of immersed samples of each group were determined by an X-ray photoelectron spectrometer (USA Thermo, Escalab Xi+) with the Al$K\alpha$ target of 1486.6 eV and voltage of 15 kV and current of 10 mA, respectively. The binding states of C1s, O1s, Mg1s, Mg2p, and Ca2p. The peak positions of each group were corrected using the C peak, which has a binding energy of 284.8 eV.

3 Results

3.1 Microstructure of Extruded Mg–2Zn–0.5Zr–0.5Nd Alloy

The metallographic microstructure of the extruded Mg–2Zn–0.5Zr–0.5Nd alloy is shown in Fig. 2a. It can be seen that the alloy organization consists of equiaxed grains dispersed along the extrusion direction. Statistical measurements show that the average grain size of the alloy is around 5 μm. Our previous work confirms that the average grain size of cast alloys is about 60 μm [39]. This indicates that the grain of the alloy is obviously refined after the hot extrusion process. This contributes to enhancing the mechanical properties and resistance to corrosion of the alloy. The XRD spectra of Mg–2Zn–0.5Zr–0.5Nd alloy are shown in Fig. 2b. The sharpest peaks can see the α-Mg phase in the

XRD spectra. The second phase can be seen as the peak corresponding to the T((MgZn)$_{92}$Nd$_8$) phase and MgZn$_2$ [35]. Furthermore, the strength of these peaks is lower than that of the substrate because of the low Nd and Zn concentrations of the alloy.

3.2 Mechanical Properties

The tensile stress–strain curves of the extruded Mg–2Zn–0.5Zr–0.5Nd alloy are displayed in Fig. 2c, d lists the mechanical property parameters. Figure 2e shows the dimensions of the tensile test sample. It is shown that the alloy has a yield strength of 229 MPa and a tensile strength of 276 MPa. The fine grain strengthening effect of polycrystalline materials is demonstrated to grow with decreasing grain size, based on the classical Hall-Page relationship ($\sigma_y = \sigma_0 + Kd^{-1/2}$) [40]. This can be demonstrated in Fig. 2a. Thus, the alloy has a high strength due to this effect. In addition, the elongation is about 20%, which indicates that the alloy exhibits good plasticity.

3.3 Stress-Life (S–N) Curves

Figure 1b displays the stress life (S–N) curves of the extruded Mg–2Zn–0.5Zr–0.5Nd alloy in HBSS with varying glucose concentrations and air. It can be seen that the fatigue limit (σ_f) of the alloy in air is about 127 MPa. The fatigue limit (σ_f) of the alloy in HBSS containing 1 g/L glucose is about 88 MPa. The fatigue limit (σ_f) of the alloy in HBSS containing 3 g/L glucose is about 70 MPa. The fatigue life is nearly linearly related to the stress amplitude. Moreover, the fatigue limit of the specimen in air is much higher than that in HBSS. The comparison of this study with the results of fatigue and CF tests on different types of Mg alloys is listed in Table 2. It can be seen that extruded alloys typically have higher fatigue strength compared to cast alloys, whether in air or solution media.

3.4 Fatigue Fracture Morphology

Figure 3 illustrates the fracture morphology of the extruded Mg-2Zn-0.5Zr-0.5Nd alloy specimens during fatigue fracture in air. As can be seen in Fig. 3a, the fracture as a whole is divided into three regions: (I) crack initiation zone, (II) crack expansion zone and (III) overload fracture zone. This is the classical fracture morphology for fatigue fracture of a specimen in air. In particular, the direction indicated by the yellow dashed arrow in the figure is the direction of fatigue crack expansion. Figure 3b shows the high magnification microscopic morphology of the crack expansion area. It can be seen that there are many wide and deep fatigue cracks along the direction of crack expansion and secondary cracks generated on its basis. In addition, from Fig. 3c, it can be
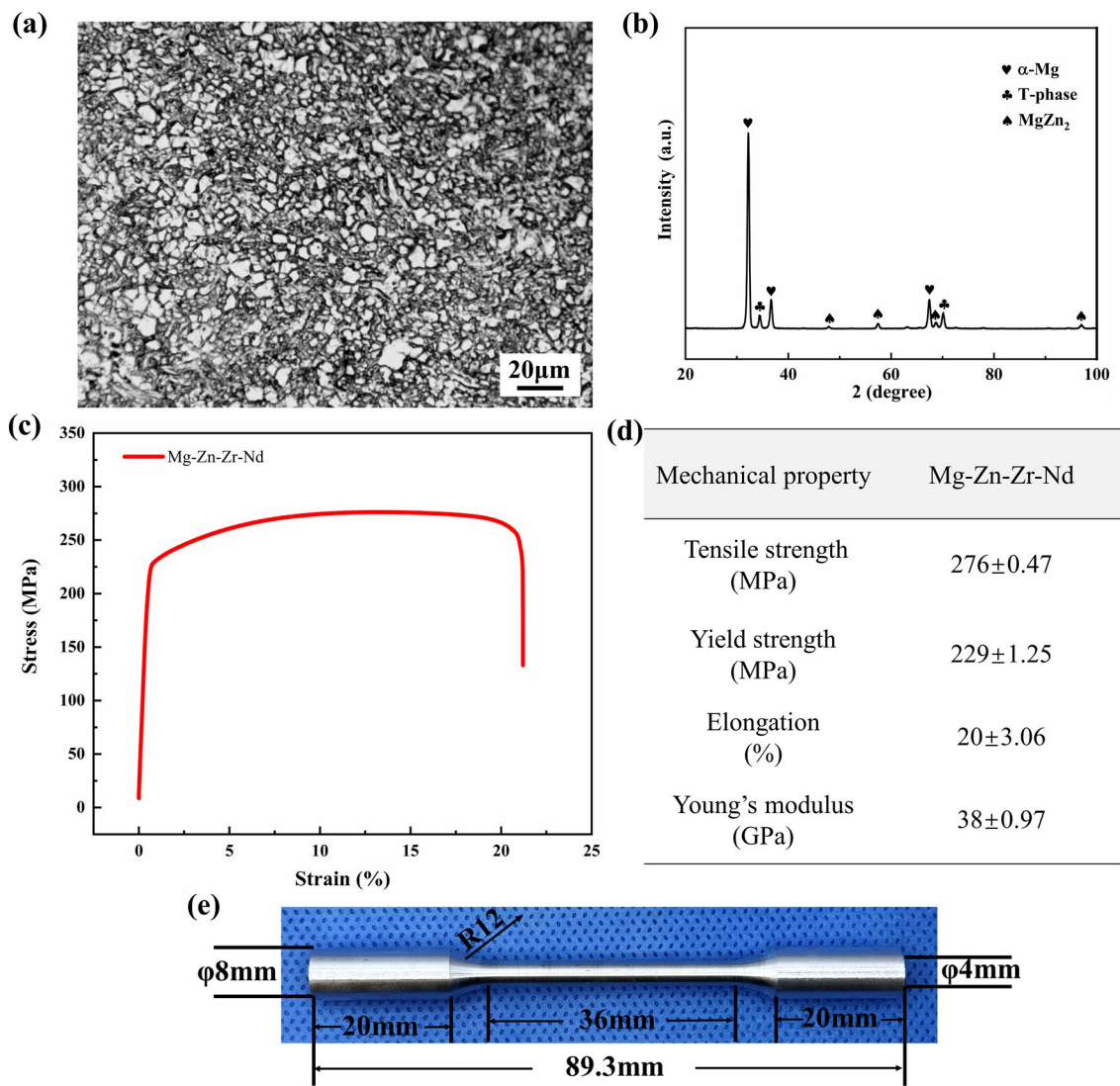
Fig. 2 Grain of the extruded Mg–2Zn–0.5Zr–0.5Nd alloy **a**, XRD phase analysis **b**, tensile stress–strain curve **c**, mechanical properties of the alloy **d**, diagram of tensile sample **e**

Table 2 Comparison of fatigue and corrosion fatigue testing of Mg alloys

| Materials	Sample type	Cycle mode	Frequency (Hz)	Medium	Fatigue strength in air (MPa)	Corrosion fatigue strength (MPa)	References
Mg–Y–Zn	As extruded	Push–pull	100	0.9% NaCl	95 ($N_f = 10^6$)	28 ($N_f = 10^6$)	[57]
AZ91D	Die-cast	–	10	SBF	50 ($N_f = 10^7$)	20 ($N_f = 10^6$)	[42]
AZ91D	Sand-cast	Fully reversed	5	m-SBF	57 ($N_f = 10^7$)	17 ($N_f = 5 \times 10^5$)	[36]
HP–Mg	As extruded	Tension–compression	10	SBF	89 ($N_f = 10^6$)	52 ($N_f = 10^6$)	[37]
Mg–2Zn–0.2Ca	As extruded	Tension–compression	10	SBF	87 ($N_f = 4 \times 10^6$)	68 ($N_f = 10^6$)	[37]
Mg–2Zn–0.5Zr–0.5Nd	As extruded	Tension–compression	2	HBSS (contains different concentrations of glucose)	127 ($N_f = 10^6$)	88, (1 g/L glucose) 70, (3 g/L glucose) ($N_f = 10^6$)	Present work
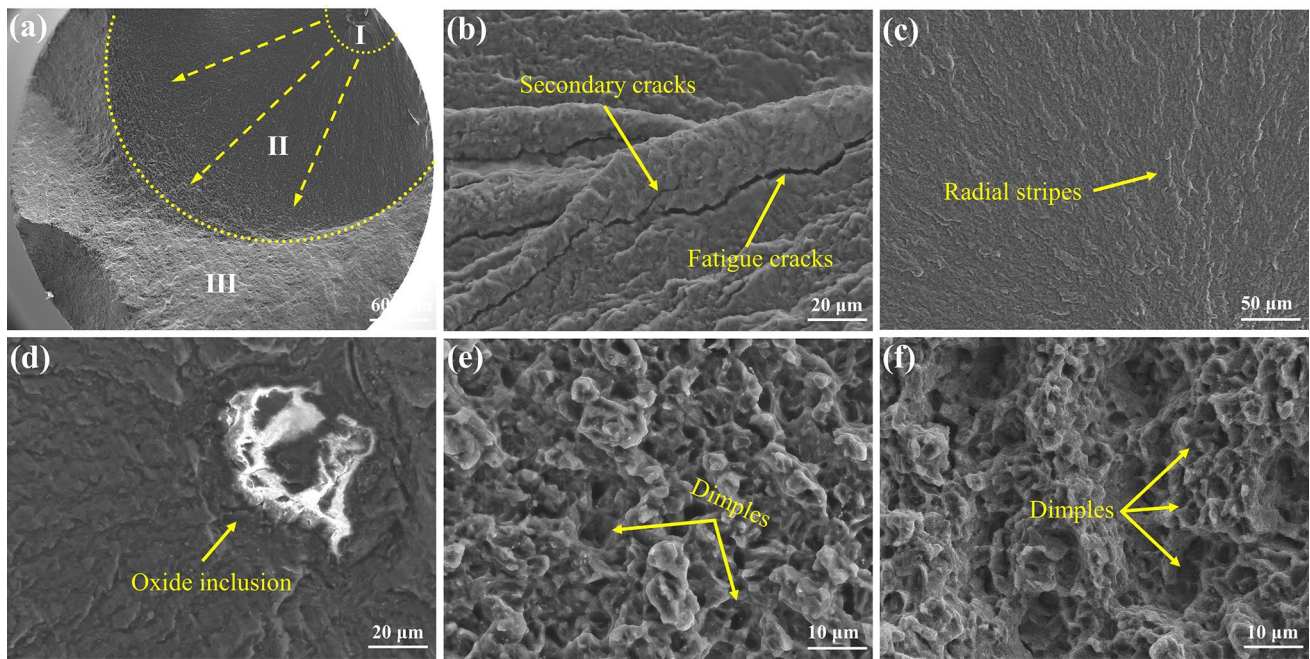
Fig. 3 Fracture morphologies of Mg–2Zn–0.5Zr–0.5Nd alloy after fatigue failure in air: **a**, **d** $\sigma = 151$ MPa, $N_f = 4.2396 \times 10^4$; **b**, **e** $\sigma = 151$ MPa, $N_f = 4.2396 \times 10^4$; **c**, **f** $\sigma = 135$ MPa, $N_f = 5.26513 \times 10^5$
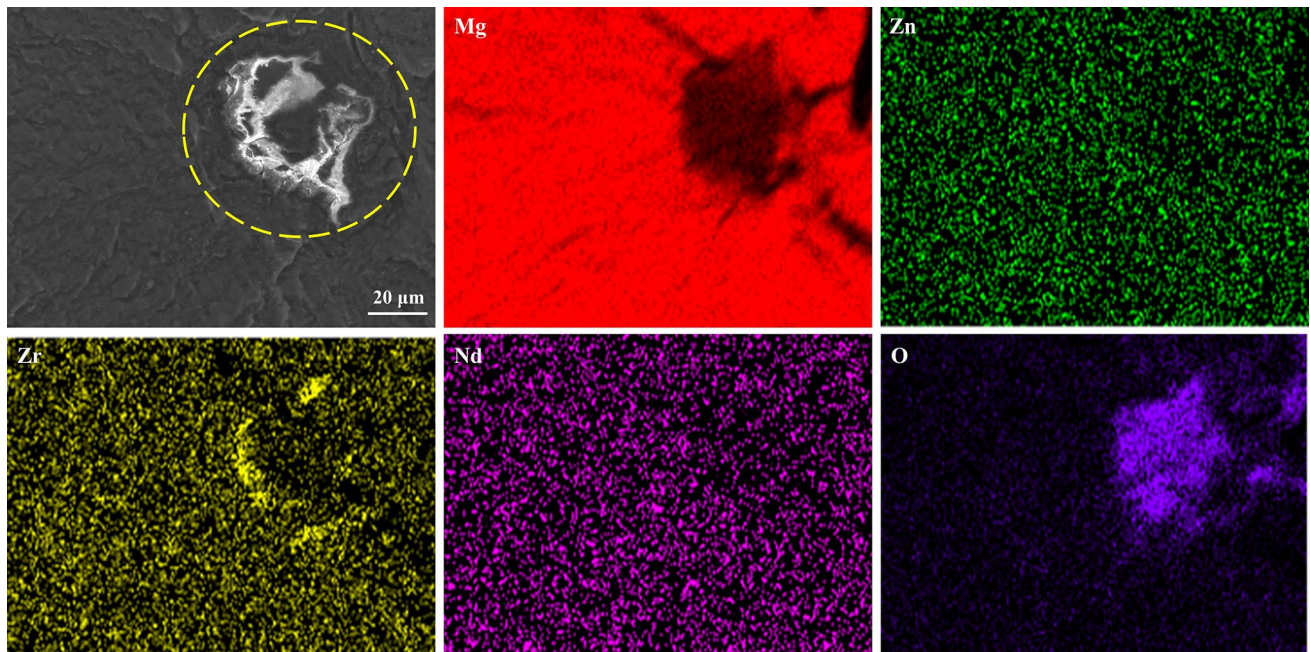

Fig. 4 SEM–EDS elemental distribution in the crack initiation zone of the fatigue fracture specimen in air ($\sigma = 151$ MPa, $N_f = 4.2396 \times 10^4$)

seen that the obvious radial river pattern morphology is lined up along the direction of crack expansion. The micromorphology of the crack sprouting region is shown in Fig. 3d. It can be seen that there is a bright white area in the figure that contrasts with the surrounding organization. Figure 4 shows the distribution of SEM–EDS elements in the bright white

region. It can be seen that the region is enriched with a large amount of oxygen, which is presumed to be MgO inclusions. It is confirmed that fatigue fracture of alloys in air with oxide inclusions is one of the common factors leading to crack initiation [18, 36]. Figure 3e, f shows that there are dimples in the overload fracture zone, which is the basis for

the judgment of ductile fracture. Furthermore, the number of dimples increases with the fatigue life of the specimen.

The fracture morphology of the specimen during fatigue fracture in HBSS containing 1 g/L glucose is displayed in Fig. 5. As can be seen in Fig. 5a, e, i, the fracture still has the typical three regions after corrosion fatigue failure. However, unlike the samples that fractured in the air, CF appeared to have multiple initial sources of fatigue (Fig. 5e). As shown in Fig. 5b, f, j, these initial sources

of fatigue are formed by pitting pits at the fracture edge. This phenomenon has also been confirmed by other studies [41–44]. It is worth noting that the more pitting pits there are, the shorter the fatigue life of the sample. The previously mentioned specimen did not break after 10^6 fatigue cycles in the air when the load was 127 MPa. Nevertheless, the fatigue life of the specimen in the solution environment was only limited to 2.3240×10^4 cycles at the identical load. This suggests that in CF testing, corrosion
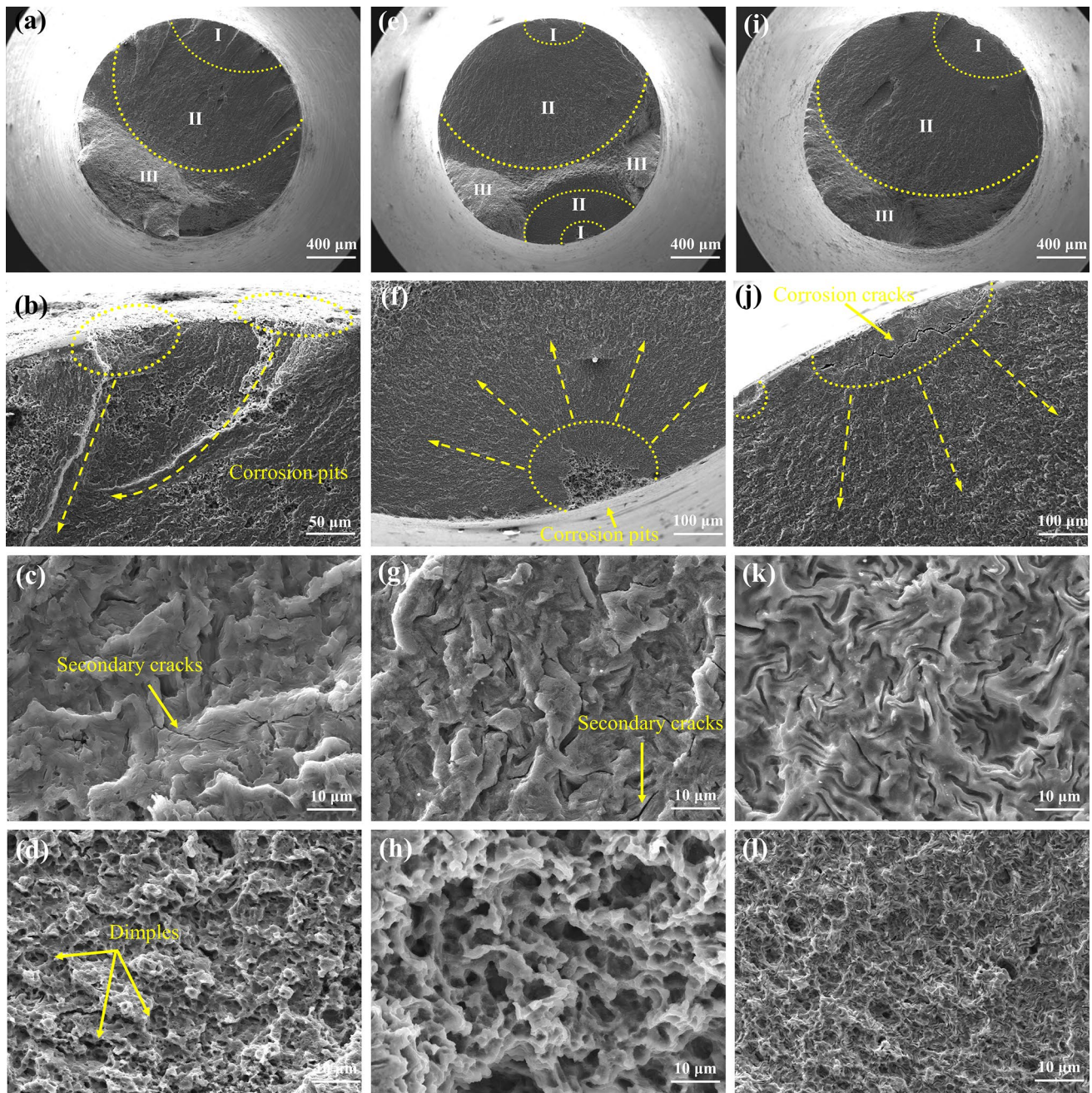

Fig. 5 Fracture morphologies of Mg–2Zn–0.5Zr–0.5Nd alloy failed by fatigue in HBSS containing 1 g/L glucose: **a–d** $\sigma = 127$ MPa, $N_f = 2.3240 \times 10^4$; **e–h** $\sigma = 111$ MPa, $N_f = 8.7085 \times 10^4$; **i–l** $\sigma = 100$ MPa, $N_f = 8.55101 \times 10^5$

of the solution has a greater effect on fatigue life [45]. In addition, the presence of the dimples can also be observed from the overloaded fracture zone in Fig. 5d, h, l. The fracture morphology of the alloy specimens after fatigue fracture in HBSS containing 3 g/L glucose is shown in Fig. 6. Unlike in HBSS containing 1 g/L glucose, the initial fatigue sources of samples that failed in HBSS containing 3 g/L glucose were corroded more severely. As shown in Fig. 6j, the edge of the fracture has a large area

of corrosion pits. In fact, as shown in Fig. 2b, the specimen did not fracture at a load of 88 MPa for 10^6 fatigue cycles when the glucose concentration was 1 g/L. However, at a glucose concentration of 3 g/L, the fatigue life was only 1.11128×10^5 cycles. This suggests that elevated glucose concentrations in the solution may accelerate the corrosion rate of the alloy, thus shortening its fatigue life. In addition, secondary cracks and tear ridges extending into the overload fracture zone were found at the crack expansion
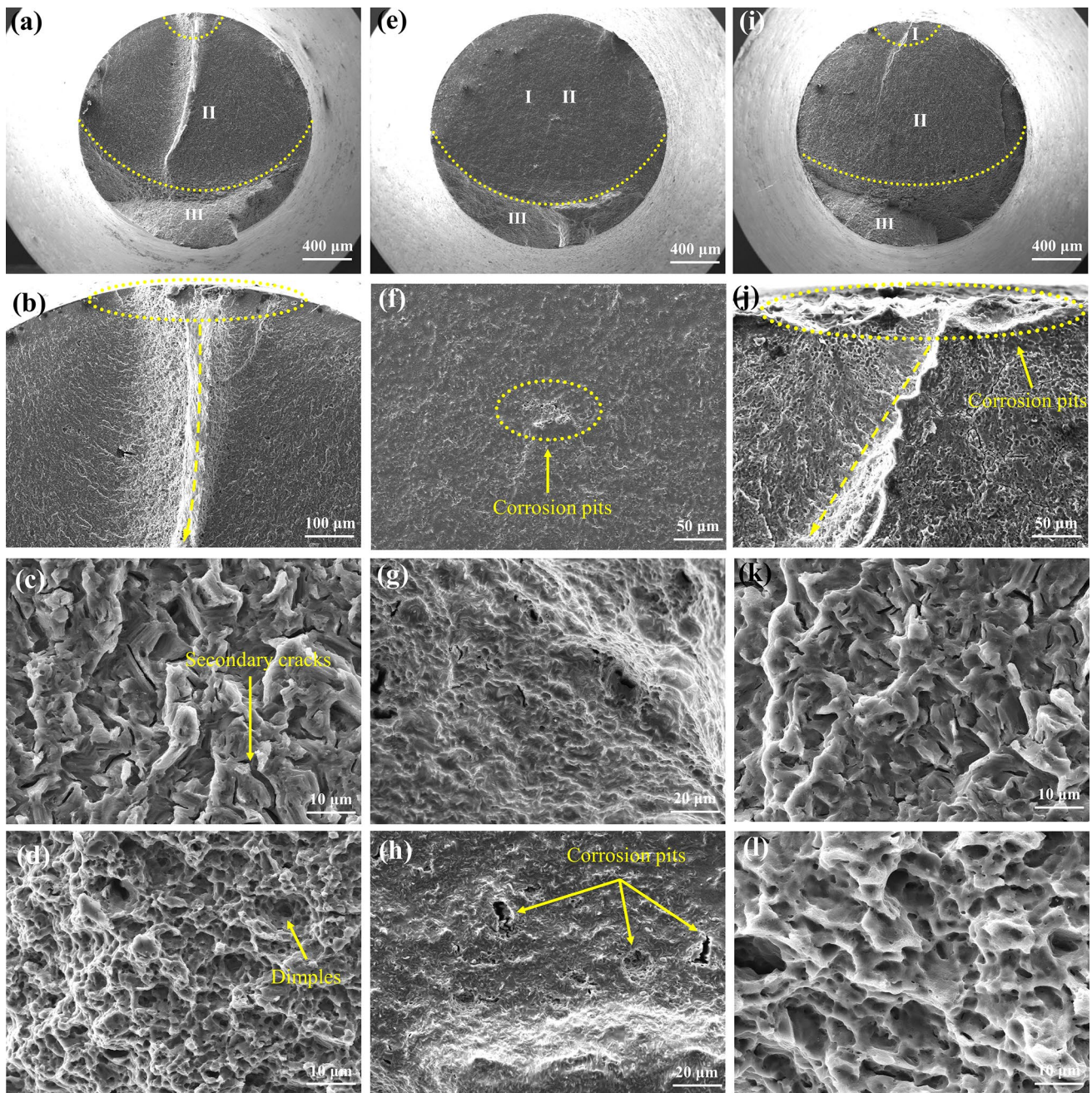

Fig. 6 Fracture morphologies of Mg–2Zn–0.5Zr–0.5Nd alloy failed by fatigue in HBSS containing 3 g/L glucose: **a–d** $\sigma = 104$ MPa, $N_f = 1.7878 \times 10^4$; **e–h** $\sigma = 88$ MPa, $N_f = 1.11128 \times 10^5$; **i–l** $\sigma = 72$ MPa, $N_f = 8.49961 \times 10^5$

area. At the same time, as shown in Fig. 6d, h, l, the dimples still exist in the overload fracture zone.

The specimen's lateral corrosion morphology following fatigue fracture in HBSS with varying glucose concentrations is shown in Fig. 7. It can be seen that the side surfaces of the samples contain a large number of pitting pits as well as corrosion pits irregularly connected by pitting pits. It is worth noting that the quantity and size of surface corrosion pits increase with the specimen's cycle life. In addition, as shown in Fig. 7f, l, long corrosion grooves arranged longitudinally in the loading direction and many elongated cracks arranged transversely in the perpendicular loading direction can be seen on the surface of the specimen. It is clear that at a glucose concentration of 3 g/L, there are more corrosion pits on the surface, and the degree of corrosion is greater. As shown in the comparison of Fig. 7e, f, k, l, when the fatigue
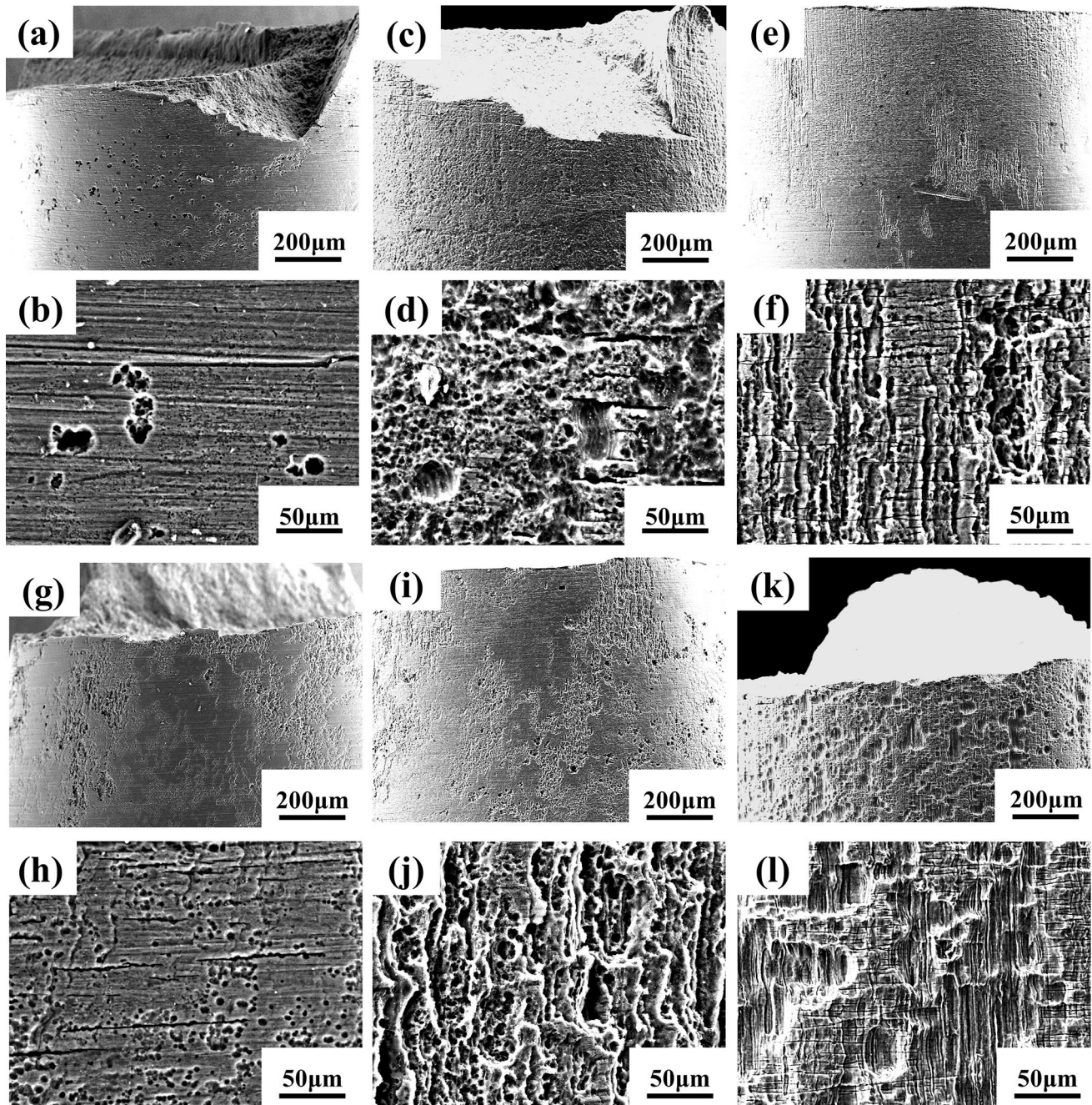

Fig. 7 Lateral corrosion morphologies of specimens after fatigue fracture in HBSS containing different concentrations of glucose: 1 g/L glucose: **a, b** $\sigma = 127$ MPa, $N_f = 2.3240 \times 10^4$; **c, d** $\sigma = 111$ MPa, $N_f = 8.7085 \times 10^4$; **e, f** $\sigma = 100$ MPa, $N_f = 8.55101 \times 10^5$; 3 g/L glucose: **g, h** $\sigma = 104$ MPa, $N_f = 1.7878 \times 10^4$; **i, j** $\sigma = 88$ MPa, $N_f = 1.11128 \times 10^5$; **k, l** $\sigma = 72$ MPa, $N_f = 8.49961 \times 10^5$

life is similar, the specimen can withstand a greater load of 100 MPa at 1 g/L glucose.

3.5 Electrochemical Performance

The potentiodynamic polarization curves of the alloy in HBSS containing different concentrations of glucose are shown in Fig. 8a. Table 3 shows the fitting results based on the polarization curves. The corrosion rate of the alloy can be calculated by the formula $P_i = 22.85 i_{corr}$ [35]. It can be seen that the corrosion current density of the samples is higher in HBSS solutions with higher glucose content (3 g/L), which indicates a relatively faster corrosion rate of the alloy. Moreover, the alloy shows a higher corrosion rate of 0.25 mm/y in HBSS with high glucose concentration. This result validates the conclusions of the corrosion fatigue
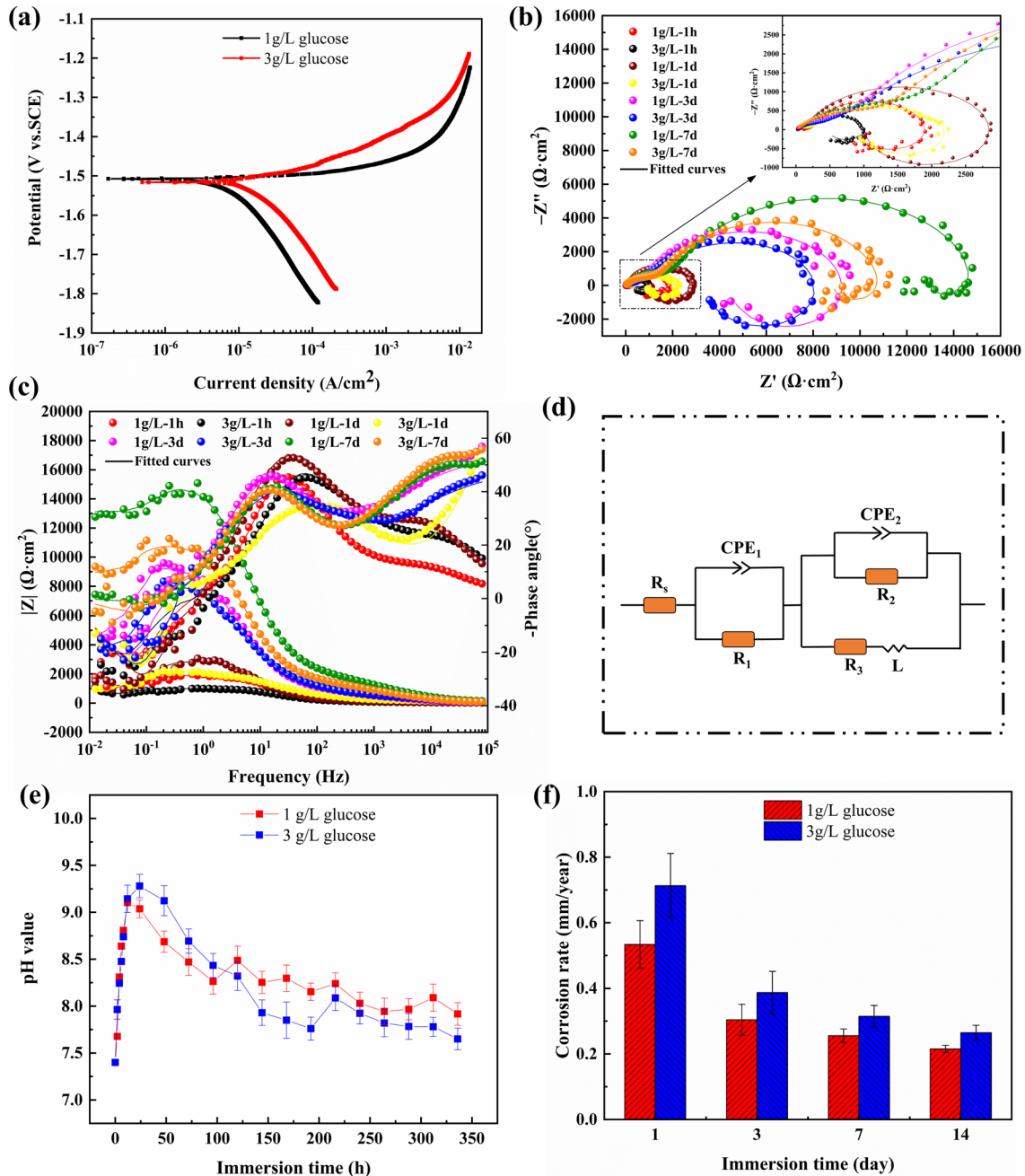

Fig. 8 Polarization curves of the alloy in HBSS containing different concentrations of glucose **a**, Nyquist plots of the alloy after immersion in HBSS containing different concentrations of glucose for 7 days **b**, Bode plots **c**, equivalent circuit **d**, pH value of the alloy after immersion in HBSS containing different concentrations of glucose for 14 days **e**, corrosion rate obtained by weight loss **f**

Table 3 Electrochemical parameters of the alloy in HBSS solution

Samples	E_{corr} (V)	I_{corr} (μA/cm^2)	Corrosion rate (mm/y)
1 g/L glucose	−1.51±0.02	6.56±0.82	0.15±0.02
3 g/L glucose	−1.52±0.01	10.9±1.15	0.25±0.03

test. Figure 8b shows the Nyquist curve of the alloy after immersion in HBSS containing different concentrations of glucose for different times. Despite the different immersion times, the Nyquist curves show the same trend which is to include two capacitive loops and one low frequency inductive loop. It can be seen that the impedance arc increases with increasing immersion time, but the magnitude of the increase is lower in the high glucose environment. The Bode plot of the alloy after immersion is shown in Fig. 8c. Typically at low frequencies, higher modulus values represent lower corrosion rates, while higher phase angles represent smoother alloy surfaces. The fitted circuit is shown in Fig. 8d. In the equivalent circuits, R_s is solution resistance, CPE_1 and R_1 represent the capacity and resistance of the corrosion product layer, respectively. CPE_2 is the double layer capacitance, R_2 is the charge transfer resistance. L is inductance and R_3 is the corresponding resistance [46]. Table 4 lists the results of EIS fitting of alloys immersed in HBSS containing different concentrations of glucose for different times. It can be found that the values of R_1 and R_2 gradually increase with the increase of immersion time, indicating that the corrosion product film becomes thicker and the charge transfer is more difficult.

3.6 Immersion Corrosion Behavior

The pH value change curves of alloys immersed in HBSS containing different concentrations of glucose for 14 days are shown in Fig. 8e. It can be seen that the pH value has a similar trend in both environments, which shows an increase and then a decrease and finally a gradual stabilization. Figure 8f shows the corrosion rate results of the alloys obtained by weight loss after immersion. It can be seen that the total weight loss of the alloy is greater at a glucose concentration of 3 g/L, indicating that high concentrations of glucose increase the corrosion rate. Figure 9 illustrates the corrosion product cross-section morphology of the alloy following immersion in HBSS containing 1 g/L and 3 g/L glucose for varying periods. By contrast, it is discovered that samples immersed in HBSS containing 3 g/L glucose had a much thicker product layer than samples immersed in 1 g/L glucose. This indicates that at a glucose concentration of 3 g/L, the alloy surface corrodes to a more significant degree; therefore, more products are generated. Moreover, the corrosion product layer's thickness tended to rise as the number of immersion days increased. Figures 10 and 11 are EDS surface scans of the cross-section corrosion product layers of Mg–2Zn–0.5Zr–0.5Nd alloy after immersion in HBSS containing 1 g/L and 3 g/L glucose for 1, 3, 7, and 14 days. Mg, O, Ca, and P constitute nearly all of the degradation products. The specific content of each element is listed in Table 5.

The X-ray photoelectron spectroscopy (XPS) spectra of the alloy's surface corrosion products are displayed in Fig. 12, which shows the following: a 7-day immersion in HBSS containing 1 g/L glucose. The full spectrum of the binding energies of each element in the corrosion products layer is shown in Fig. 12a, where it can be observed that the major elements are C, O, Mg, Ca, and P. As shown in Fig. 12b, it can be seen that the main peak binding energy of C1s is 284.6 eV, corresponding to hydrocarbon substances with characteristic binding energies (C−C/C−H). The split peak, which has a binding energy of 285.80 eV, might be associated with C–O [24]. Furthermore, a third signal at 289 eV was observed, which could be connected to the –COO$^-$group [47]. In Fig. 12c, the O1s can be split peak fitted to synthesize two spectra with peaks located at 531.2 eV and 532.6 eV, which are associated with MgO and Mg(OH)$_2$, respectively [48]. As shown in Fig. 12d, the binding energy of the main peak of Mg1s is 1303.5 eV, and the peak with a binding energy of 1303.9 eV corresponds to the product MgO. As shown in Fig. 12e for Mg2p, there are two peaks at binding energies of 49.4 eV and 50.2 eV,

Table 4 Fitted EIS parameters of alloys immersed for 7 days in HBSS containing different concentrations of glucose

| Conditions	R_s (Ω·cm^2)	CPE_1 (Ω^{-1}·cm^{-2}·s^n)	n_1	R_1 (Ω·cm^2)	CPE_2 (Ω^{-1}·cm^{-2}·s^n)	n_2	R_2 (Ω·cm^2)	R_3 (Ω·cm^2)	L (H·cm^{-2})
1 g/L-1 h	17.27	1.45×10^{-5}	0.68	187.9	1.21×10^{-5}	0.94	1.62×10^3	874.8	5.06×10^3
3 g/L-1 h	18.31	1.89×10^{-5}	0.60	145.5	1.92×10^{-5}	0.90	846.6	504	3.05×10^3
1 g/L-1 d	17.6	2.6×10^{-5}	0.62	142.2	1.48×10^{-5}	0.86	2.8×10^3	1.23×10^3	3.44×10^3
3 g/L-1 d	19.1	1.3×10^{-5}	0.87	155.1	3.16×10^{-5}	0.62	2.2×10^3	1.24×10^3	5.75×10^3
1 g/L-3 d	16.8	6.62×10^{-6}	0.60	781.7	1.08×10^{-5}	0.78	9.03×10^3	3.24×10^4	6.2×10^3
3 g/L-3 d	19.2	8.11×10^{-6}	0.79	645	1.44×10^{-5}	0.70	8.32×10^3	4.04×10^4	4.19×10^3
1 g/L-7 d	18.52	2.27×10^{-6}	0.61	2.07×10^3	4.76×10^{-6}	0.83	1.33×10^4	6.48×10^4	7.27×10^4
3 g/L-7 d	20.37	2.85×10^{-6}	0.63	1.53×10^3	7.07×10^{-6}	0.84	9.62×10^3	3.15×10^4	7.42×10^4
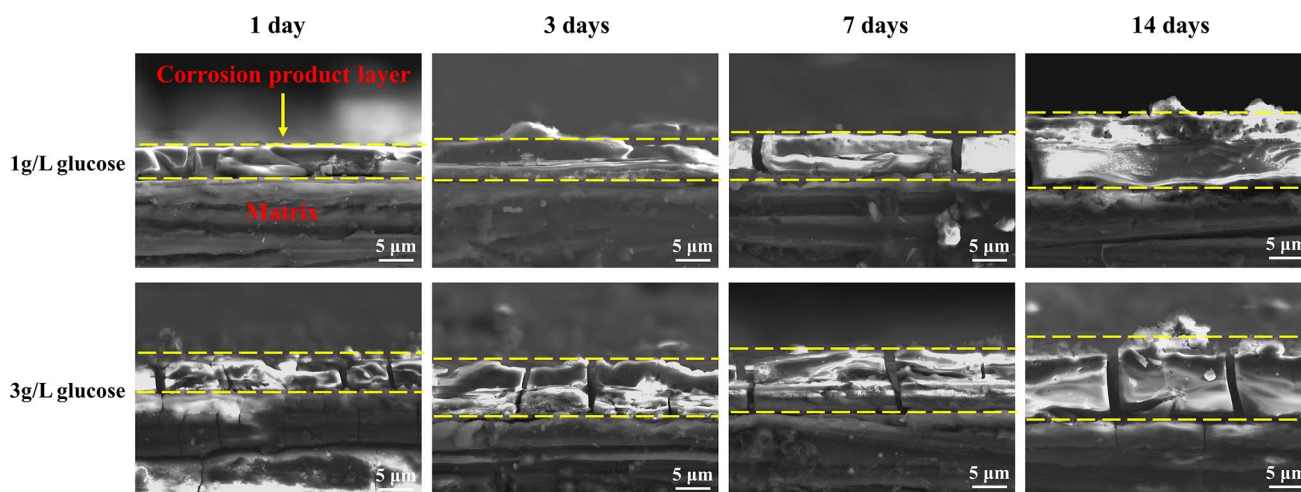
Fig. 9 SEM photographs of cross-sectional corrosion product layers of Mg–2Zn–0.5Zr–0.5Nd alloy after immersion in HBSS containing 1 g/L glucose and 3 g/L glucose for 1, 3, 7 and 14 days
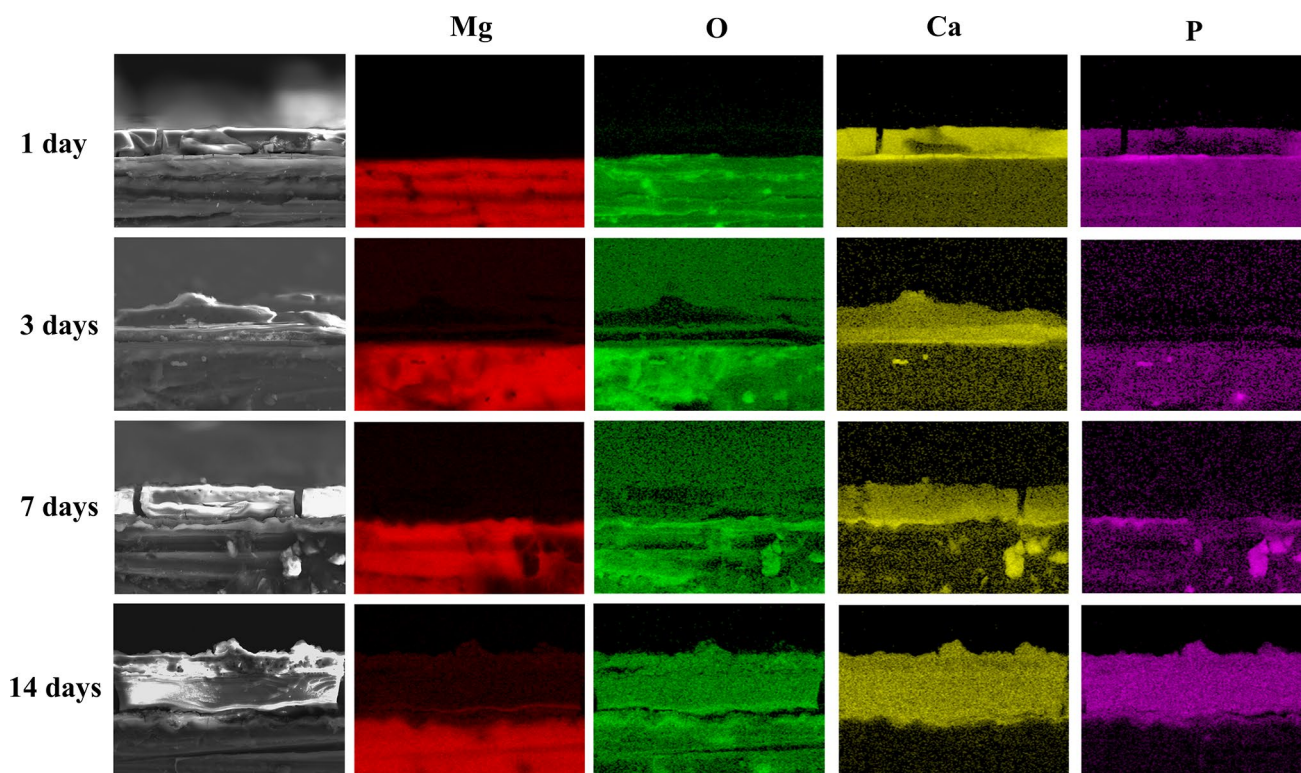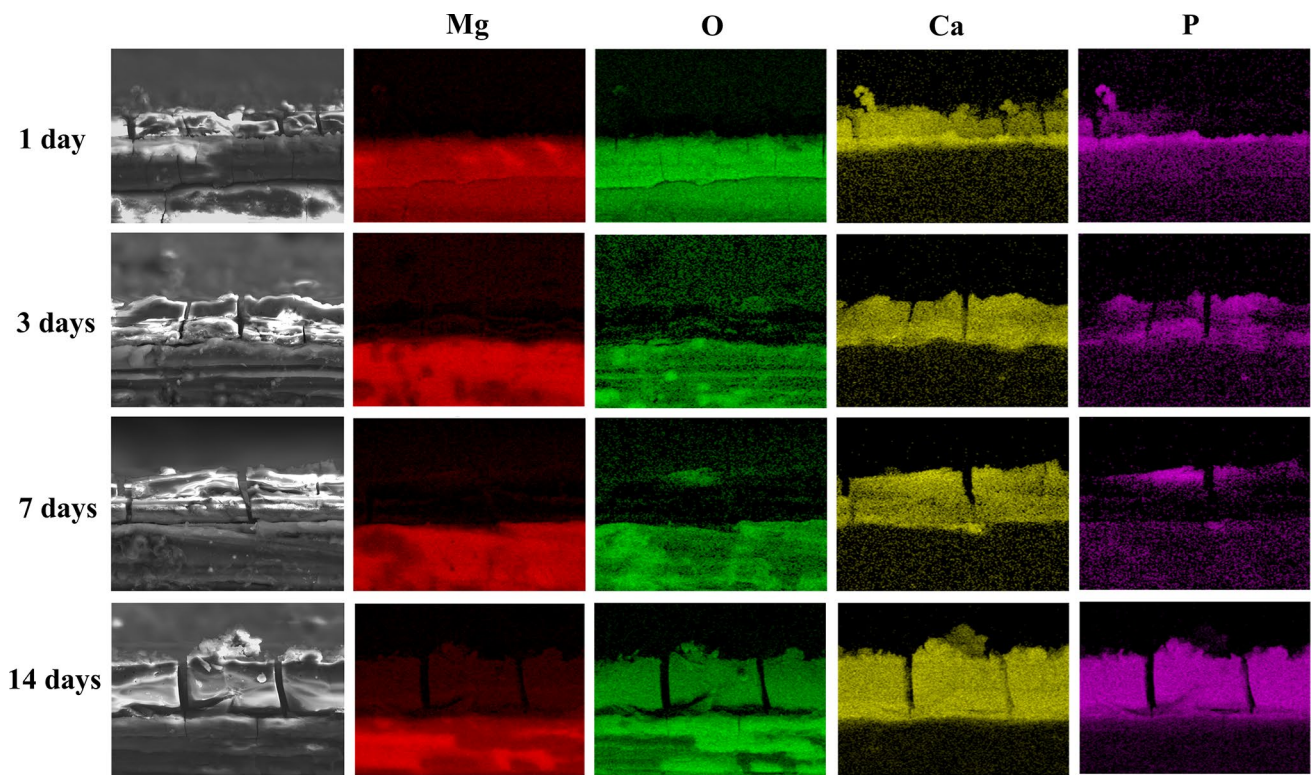

Fig. 10 EDS surface scanning of cross-section corrosion product layers of Mg–2Zn–0.5Zr–0.5Nd alloy after immersion in HBSS containing 1 g/L glucose for 1, 3, 7 and 14 days

corresponding to $Mg(OH)_2$ and $(-COO)_2$ Mg, respectively [24, 48]. In Fig. 12f, two peaks of Ca2p are present at 347.2 eV and 351.1 eV, corresponding to $Ca_3(PO_4)_2$ and $CaCO_3$, respectively.

Figure 13 shows the XPS spectra of surface corrosion products of the alloy after of 7 days immersion in HBSS

containing 3 g/L glucose. It can be seen that the signal of the C1s peak in the full spectrum is enhanced with increasing glucose concentration, and there is also a slight increase in the signal of the $-COO^-$, C−O, and(C−C/C−H) group peak in Fig. 13b. It is noteworthy that the scan of Mg2p in Fig. 13e shows a significant enhancement of the

Fig. 11 EDS surface scanning of cross-section corrosion product layers of Mg–2Zn–0.5Zr–0.5Nd alloy after immersion in HBSS containing 3 g/L glucose for 1, 3, 7 and 14 days

Table 5 EDS surface scanning elemental composition of cross-section corrosion product layers of Mg–2Zn–0.5Zr–0.5Nd alloy after immersion in HBSS containing different concentrations of glucose

Condition	Elemental composition (wt%)			
	Mg	O	Ca	P
1 g/L-1 d	84.3	5.7	4.2	0.6
1 g/L-3 d	65.6	15.4	3.2	0.5
1 g/L-7 d	41.8	33.5	11.9	3.1
1 g/L-14 d	36.6	31.5	17.3	9.9
3 g/L-1 d	36.6	43.9	8.3	2.3
3 g/L-3 d	62.4	12.5	9.4	2.3
3 g/L-7 d	67.3	16.9	8.5	1.3
3 g/L-14 d	51.7	19.4	14.9	9.5

$(-COO)_2$ Mg peak signal and a weakening of the $Mg(OH)_2$ peak. This suggests that the high concentration of glucose in solution may have a destructive effect on the $Mg(OH)_2$ layer. By analyzing the content of each element of EDS shown in Table 5 and the XPS results, it is presumed that the corrosion products on the surface of the alloy are mainly composed of MgO, $Mg(OH)_2$, $(-COO)_2$ Mg, and minor Ca-P compounds. The elements and composition of the corrosion product layer are, in general, consistent with most of the results reported

in previous research on the degradation of Mg alloys in simulated body fluids. Bornapour et al. [49] investigated the corrosion of pure Mg and Mg-Sr alloys in simulated body fluids and revealed that $Mg(OH)_2$, hydroxyapatite, and trace levels of $CaCO_3$ were the main components of the corrosion layer. Ascencio et al. [50] studied the degradation products of WE43 Mg alloy in m-SBF consisting of a mixture of amorphous $Mg(OH)_2$ and carbonate apatite.

4 Discussion

4.1 Fatigue Property

The fatigue life curves of the alloy are shown in Fig. 5. The S–N curve fitting equation in Fig. 2b is given in the following equation (semi-logarithmic).

$$y = a \cdot x^b, \tag{1}$$

where y and x are σ_{max} and log N_f, respectively. σ_{max} is the maximum applied stress, and N_f is the number of cycles to failure at a certain stress level. The parameters a and b are the coefficients. The equation obtained after fitting is as follows:
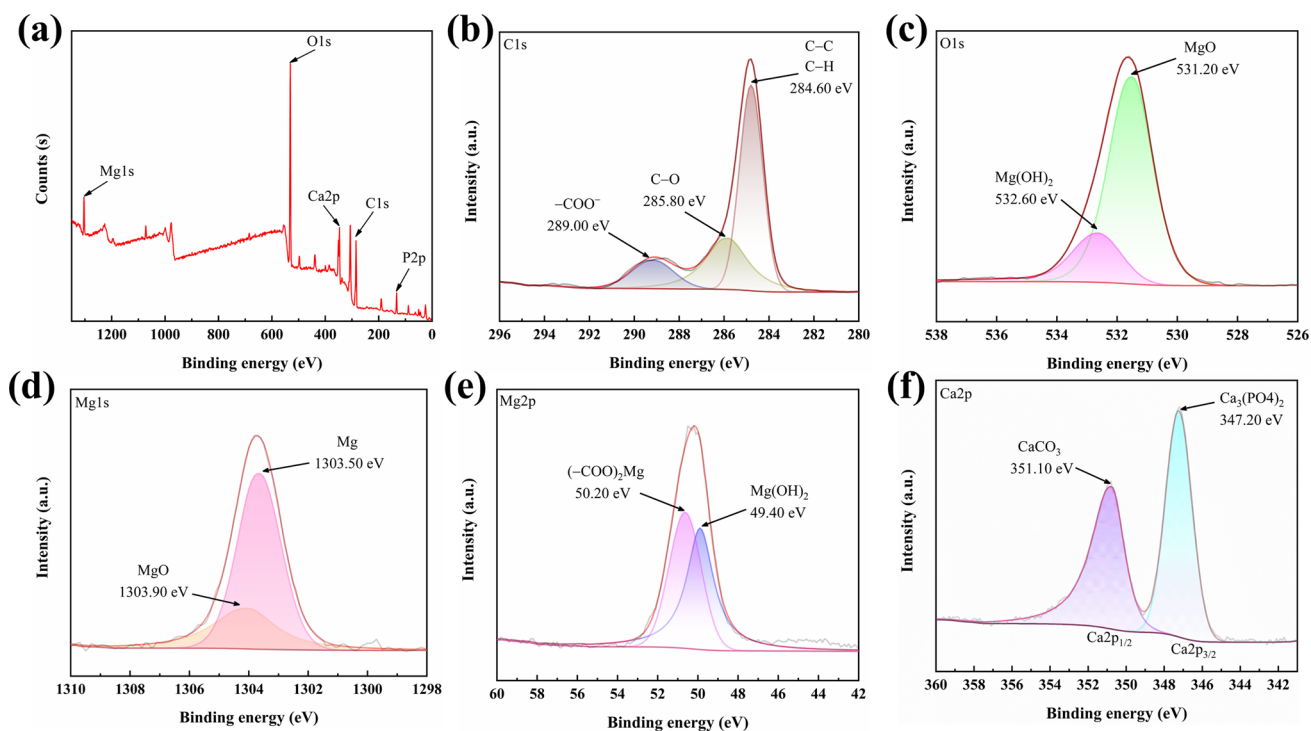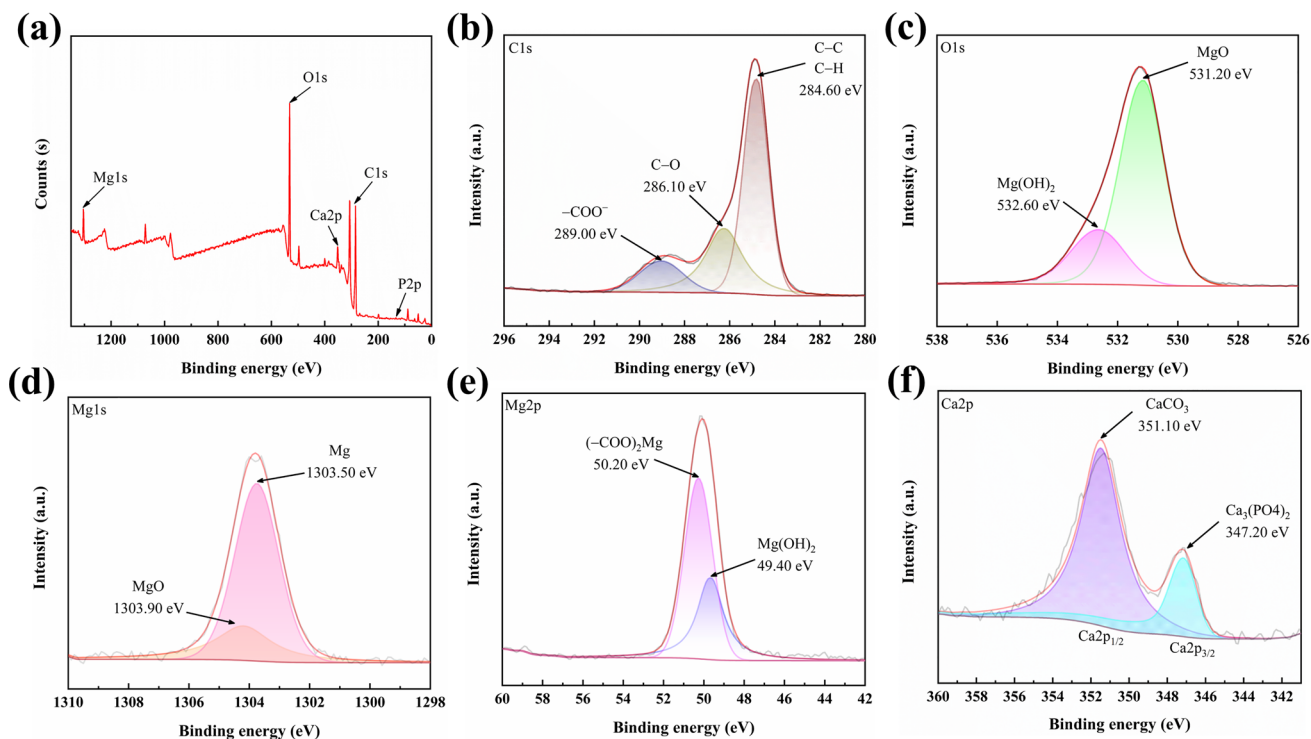
Fig. 12 XPS spectra of corrosion products of Mg–2Zn–0.5Zr–0.5Nd alloy after 7 days immersion in HBSS containing 1 g/L glucose: total energy spectrum **a**, C1s **b**, O1s **c**, Mg1s **d**, Mg2p **e**, Ca2p **f**

Fig. 13 XPS spectra of corrosion products of Mg–2Zn–0.5Zr–0.5Nd alloy after 7 days immersion in HBSS containing 3 g/L glucose: total energy spectrum **a**, C1s **b**, O1s **c**, Mg1s **d**, Mg2p **e**, Ca2p **f**

$$\text{In air} : y = 289.57 \cdot x^{-0.06}, \tag{2}$$

$$\text{In HBSS with 1 g/L glucose} : y = 243.97 \cdot x^{-0.07}, \tag{3}$$

$$\text{In HBSS with 3 g/L glucose} : y = 254.23 \cdot x^{-0.10}. \tag{4}$$

Because of the combined effects of cyclic loading and corrosive media, the fatigue resistance of the specimen in HBSS is significantly lower than in air when the medium is a solution. Moreover, the fatigue performance of the samples in HBSS with a higher glucose concentration was worse than in normal concentration, as well as in the solution environment. Bhuiyan et al. [41] evaluated the rate of reduction in fatigue strength of extruded AZ61 Mg alloy by the $(\sigma_{LH} - \sigma_{CE})/\sigma_{LH}$ ratio, where σ_{LH} is the fatigue limit under low humidity conditions, and σ_{CE} is the fatigue limit under corrosive media. Therefore, accordingly, the effect of a corrosive environment on fatigue strength in this study can be expressed by the following equation:

$$\frac{\sigma_{air} - \sigma_{HBSS}}{\sigma_{air}}, \tag{5}$$

where σ_{air} represents the fatigue strength in air and σ_{HBSS} represents the fatigue strength in a HBSS environment. A 31% reduction in fatigue strength was calculated when the medium was a HBSS containing 1 g/L glucose. It is known that Mg alloys are susceptible to pitting in solutions containing Cl^- ions, including simulated body fluids, which is the main reason for the significant reduction in fatigue properties of the alloys in HBSS [36]. When the medium was HBSS containing 3 g/L glucose, the fatigue strength was reduced by 45%. This suggests that the corrosive environment affects the fatigue behavior of materials largely and that high concentrations of glucose can promote the corrosion of the alloy and the expansion of CF cracks by some mechanism.
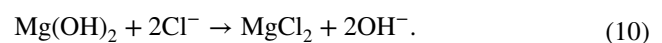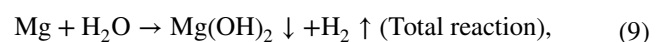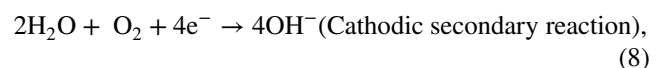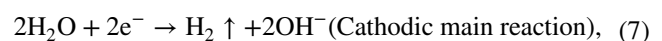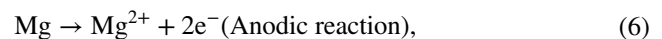
4.2 Corrosion Performance

Mg alloys are known to be highly susceptible to aggressive chloride ions in solution media, leading to increased corrosion [51]. During the testing of this study, it was found that the alloy was prone to pitting as soon as it entered the HBSS. As shown in Fig. 7h, many pitting pits appeared on the fracture side of the alloy after only 1.7878×10^4 corrosion fatigue cycles (about 2.5 h). Electrochemical results show the same trend, with smaller impedance arcs in the pre-immersion period and the presence of a nearly completely closed inductive loop. However, the corrosion product layer on the surface of the alloy gradually accumulates as the immersion time increases (Fig. 9). As can be seen from Fig. 8b and Table 4, the impedance arc gradually increases

from the time period of 1 h to 7 d of immersion, and the values of R_1 and R_2 show an increasing trend. This indicates that the protective effect of the corrosion product film slows down the corrosion rate on the alloy surface. And, as can also be seen in Fig. 8f, the corrosion rate of the alloys obtained by weight loss is gradually decreasing from 1 to 14 d of immersion. The rate of weight loss corrosion is slightly higher compared to the corrosion rates obtained from the electrochemical tests as shown in Table 3, probably due to the different time points of immersion. However, it is worth noting that both electrochemical and weight loss results show that the overall corrosion rate of the alloy is greater in a high glucose environment (containing 3 g/L glucose HBSS). This is also verified by more and deeper corrosion pits on the side of the fatigue fracture in Fig. 7. These conclusions are in agreement with the results of the S–N curve shown in Fig. 2b, in which the corrosion fatigue performance of the alloy decreases in high glucose environments.

4.3 Fatigue Failure Mechanism

It is well known that the fatigue damage of alloys in air is mainly attributed to the mechanical properties of the material itself and the presence of internal defects such as inclusions. However, when the medium becomes a solution environment, the fatigue properties of the alloy are greatly affected by the corrosive fluid, and the mechanism of fatigue crack nucleation and expansion becomes more complex. Figure 14 shows the failure mechanism of Mg–2Zn–0.5Zr-0.5Nd alloy in HBSS containing glucose. According to Eqs. (6–8), Mg dissolution reactions and micro-galvanic corrosion reactions occur when the alloy is immersed in solution. Subsequently, Eq. (9) causes the surface of the sample to develop a somewhat protective $Mg(OH)_2$ film. However, Cl^- in solution can attack the $Mg(OH)_2$ film and react with it to generate the more soluble $MgCl_2$ (Eq. 10). The specific reaction formulae involved are shown below [52–55]:

$$Mg \rightarrow Mg^{2+} + 2e^- \text{(Anodic reaction)}, \tag{6}$$

$$2H_2O + 2e^- \rightarrow H_2 \uparrow + 2OH^- \text{(Cathodic main reaction)}, \tag{7}$$

$$2H_2O + O_2 + 4e^- \rightarrow 4OH^- \text{(Cathodic secondary reaction)}, \tag{8}$$

$$Mg + H_2O \rightarrow Mg(OH)_2 \downarrow + H_2 \uparrow \text{(Total reaction)}, \tag{9}$$

$$Mg(OH)_2 + 2Cl^- \rightarrow MgCl_2 + 2OH^-. \tag{10}$$

As shown in Fig. 14a, the reaction of phosphate ions present in solution with calcium ions also produces Ca-P compounds. In addition, the presence of $CaCO_3$ was found
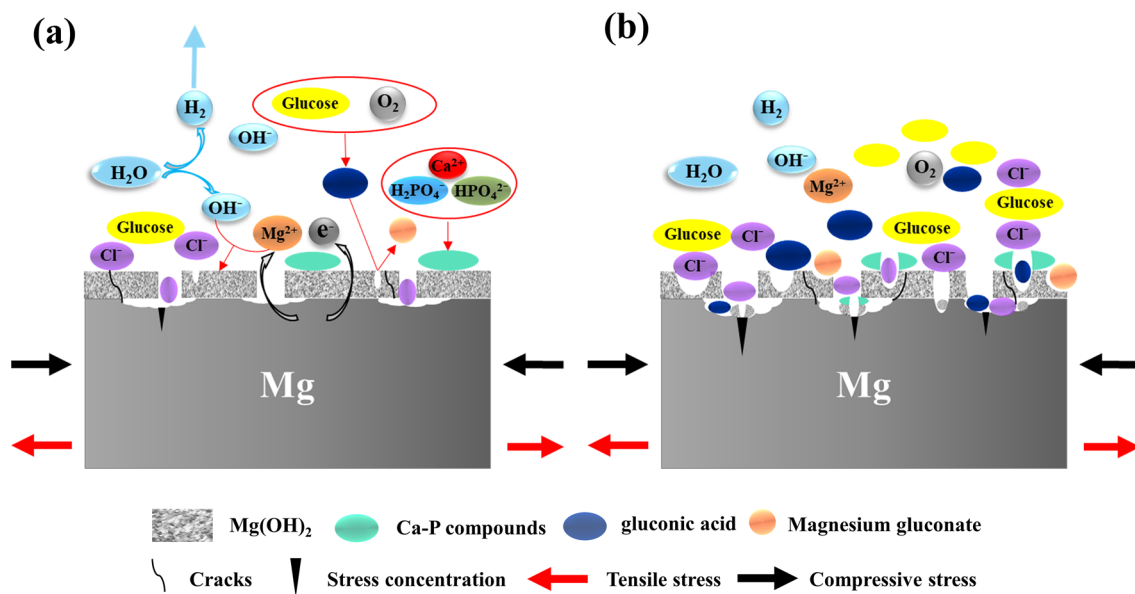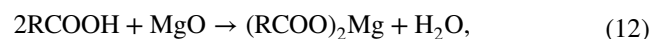
Fig. 14 Failure mechanism diagram of Mg–2Zn–0.5Zr–0.5Nd alloy in HBSS containing glucose: low-glucose environment **a**, high-glucose environment **b**

in the XPS results, as shown in Fig. 12f. However, the content of these elements in HBSS is low, so the compounds formed have a limited protective effect on the alloy substrate. On the one hand, since the corrosion medium is constantly flowing during the corrosion fatigue process of the alloy, the corrosion products on the side surfaces need to be better adhered. They cannot effectively block the intrusion of ions in the corrosion medium on the sample surface. On the other hand, in the second phase, impurities and cyclic loading cause electrochemical inhomogeneities on the surface of the alloy, which provide conditions for the formation of pitting pits [56]. In the matrix by the corrosive medium in the continuous process of scouring, local corrosion site expansion, when a local corrosion site size reaches a critical value, in the cyclic stress will soon occur under the action of stress concentration. At the same time, the penetration of Cl$^-$ ions leads to an increasing number of nucleation sites in the microcracks.

Actually, the glucose has a strong adsorption and adhesion capacity to adsorb large amounts of Cl$^-$ ions to the sample surface to react with the corrosion product film. As a result, the protective Mg(OH)$_2$ layer is gradually destroyed and Fig. 14b illustrates this process. According to Zeng et al. [24], The functional group of glucose is derived from Carbon #1 (the isomeric carbon) and is the center of the hemiacetal functional group, which has both an oxygen and an alcohol group. Glucose's aldehyde group (CH$_2$OH(CHOH)$_4$CHO) is very active and can be oxidized to create gluconic acid (CH$_2$OH(CHOH)$_4$COOH) (Eq. 11). The lower pH in the high-glucose environment shown in Fig. 8e can also confirm this result. As a result, gluconic acid destroys the Mg(OH)$_2$

film together with corrosive Cl$^-$ ions, thus accelerating the corrosion process of Mg. At the same time, a precipitate of magnesium gluconate ((CH$_2$OH(CHOH)$_4$COO)$_2$ Mg) is generated on the surface of Mg, as shown in Eq. (12) and (13). This can be confirmed by the XPS scans shown in Fig. 12e. The reaction formulae involved due to the addition of glucose are as follows [24, 30]:

$$RCHO \rightarrow RCOOH, \tag{11}$$

$$2RCOOH + MgO \rightarrow (RCOO)_2Mg + H_2O, \tag{12}$$

$$2RCOOH + Mg(OH)_2 \rightarrow (RCOO)_2Mg + 2H_2O, \tag{13}$$

where R is the CH$_2$OH(CHOH)$_4^-$ group from CH$_2$OH(CHOH)$_4$CHO.

As the concentration of glucose in solution increases, so does the amount of (CH$_2$OH(CHOH)$_4$COOH) produced by oxidation, and therefore the amount of (−COOH) converted. This is confirmed by the signal enhancement of the (−COO)$_2$ Mg peak, and the weakening of the signal intensity of the Mg(OH)$_2$ peak as shown in Fig. 13e. The metal adsorbs reactive substances throughout the reaction process, which weakens its mechanical properties, reduces its surface energy, and facilitates the production of corrosion fatigue fractures, according to the hypothesis of corrosion fatigue adsorption [34]. Furthermore, the affinity of glucose with Mg^{2+} was higher than that with glucose with Ca^{2+} based on the metal ion affinities (MIAs) calculated from density flooding theory (DFT). This suggests that glucose may preferentially react with Mg^{2+} in HBSS [25].

Consequently, the synergistic attack of adsorbed Cl⁻ ions and gluconic acid leads to the loss of protective properties of the $Mg(OH)_2$ film and the creation of progressively larger crevices. Subsequently, the solution penetrates the alloy matrix through the crevices, and a new corrosion process continues. With the stress loading and corrosion reaction, pitting and microcracks on the alloy surface gradually increase to produce stress concentration. As a result, as the concentration of glucose in the HBSS increases, the alloy corrodes more severely and has a greater tendency to fatigue failure.

5 Conclusions

In this work, the fatigue properties of extruded Mg–Zn–Zr–Nd alloy in air and HBSS containing different concentrations (1 g/L and 3 g/L) of glucose were investigated. Some of this study's findings are listed here.

1. The fatigue strength of Mg–Zn–Zr–Nd alloy loaded cyclically in the air for 10^6 cycles without fracture is 127 MPa, while in the HBSS containing 1 g/L glucose and 3 g/L glucose were 88 MPa and 70 MPa, respectively. The source of fatigue cracking of alloys in air is oxide particle inclusions, while the source of fatigue cracking in HBSS is corrosion pits.
2. When the alloy is in a highly concentrated glucose solution, glucose adsorbs large amounts of aggressive Cl⁻ ions, which accelerates the corrosion process. In addition, glucose can be oxidized under certain conditions to form gluconic acid, which then reacts with $Mg(OH)_2$ to form magnesium gluconate, thereby destroying the protective film of corrosion products.
3. In air, the fatigue fracture is presumed to be a ductile fracture mode due to the presence of a large number of dimples in the mechanical overload zone of the fatigue fracture. In contrast, only a few dimples were found in glucose-containing simulated body fluids, which are presumed to be a combination of ductile and brittle fractures.

Declarations

Conflict of interest The authors state that there are no conflicts of interest to disclose.

References

[1] S. Abazari, A. Shamsipur, H.R. Bakhsheshi-Rad, J. Magnes. Alloy. **10**, 3612 (2022)
[2] D. Zhao, F. Witte, F. Lu, J. Wang, J. Li, L. Qin, Biomaterials **112**, 287 (2017)
[3] H.R. Bakhsheshi-Rad, E. Hamzah, H.T. Low, M.H. Cho, M. Kasiri-Asgarani, S. Farahany, A. Mostafa, M. Medraj, Acta Metall. Sin. -Engl. Lett. **30**, 201 (2017)
[4] M.S. Song, R.C. Zeng, Y.F. Ding, R.W. Li, M. Easton, I. Cole, N. Birbilis, X.B. Chen, J. Mater. Sci. Technol. **35**, 535 (2019)
[5] N. Wang, S. Yang, H. Shi, Y. Song, H. Sun, Q. Wang, L. Tan, S. Guo, J. Magnes. Alloy. **10**, 3327 (2022)
[6] L. Lei, Z. Cui, H. Pan, K. Pang, X. Wang, H. Cui, Corros. Sci. **195**, 109975 (2022)
[7] C. Liu, X. Chen, Y. Wu, Y. Hu, W. Zhang, Y. Zhang, J. Bai, F. Pan, Acta Metall. Sin. -Engl. Lett. **36**, 1281 (2023)
[8] D. Zhang, Q. Han, K. Yu, X. Lu, Y. Liu, Z. Lu, Q. Wang, J. Mater. Sci. Technol. **61**, 33 (2021)
[9] X. Zhou, Q. Zhang, J. Lu, Y. Zheng, L. Wu, D. Xu, X. Zhang, Q. Wang, Acta Metall. Sin. -Engl. Lett. **36**, 1961 (2023)
[10] J.L. Wang, J.K. Xu, C. Hopkins, D.H. Chow, L. Qin, Adv. Sci. (Weinh) **7**, 19024 (2020)
[11] A. Yamamoto, S. Hiromoto, Mater. Sci. Eng. C **29**, 1559 (2009)
[12] Y. Shao, R.C. Zeng, S.Q. Li, L.Y. Cui, Y.H. Zou, S.K. Guan, Y.F. Zheng, Acta Metall. Sin. -Engl. Lett. **33**, 615 (2020)
[13] X. Li, X. Liu, S. Wu, K.W.K. Yeung, Y. Zheng, P.K. Chu, Acta Biomater. **45**, 2 (2016)
[14] S. Agarwal, J. Curtin, B. Duffy, S. Jaiswal, Mater. Sci. Eng. C Mater. Biol. Appl. **68**, 948 (2016)
[15] H.Y. Niu, F.F. Cao, K.K. Deng, K.B. Nie, J.W. Kang, H.W. Wang, Acta Metall. Sin. -Engl. Lett. **33**, 362 (2019)
[16] S. Abazari, A. Shamsipur, H.R. Bakhsheshi-Rad, J.W. Drelich, J. Goldman, S. Sharif, A.F. Ismail, M. Razzaghi, J. Magnes. Alloy. **11**, 2655 (2023)
[17] R.K.S. Raman, S.E. Harandi, Materials (Basel) **10**, 1316 (2017)
[18] S. Jafari, S.E. Harandi, R.K. Singh Raman, JOM **67**, 1143 (2015)
[19] R.K. Singh Raman, S. Jafari, S.E. Harandi, Eng. Fract. Mech. **137**, 97 (2015)
[20] R.C. Zeng, Y. Hu, S.K. Guan, H.Z. Cui, E.H. Han, Corros. Sci. **86**, 171 (2014)
[21] S. Cabeza, P. Pérez Zubiaur, G. Garcés, C. Andrade, P. Adeva, Metals. **10**, 148 (2020)
[22] Y. Jang, B. Collins, J. Sankar, Y. Yun, Acta Biomater. **9**, 8761 (2013)
[23] F. Witte, Acta Biomater. **6**, 1680 (2010)
[24] R.C. Zeng, X.T. Li, S.Q. Li, F. Zhang, E.H. Han, Sci. Rep. **5**, 13026 (2015)
[25] Y. Liu, Z. Liu, L. Liu, H. Xue, Q. Wang, D. Zhang, Adv. Eng. Mater. **23**, 2001451 (2021)
[26] Y. Wang, L.Y. Cui, R.C. Zeng, S.Q. Li, Y.H. Zou, E.H. Han, Materials **10**, 725 (2017)
[27] W. Yan, Y.J. Lian, Z.Y. Zhang, M.Q. Zeng, Z.Q. Zhang, Z.Z. Yin, L.Y. Cui, R.C. Zeng, Bioact. Mater. **5**, 318 (2020)
[28] S. Liu, B. Wang, J. Mater. Res. Technol. **9**, 6612 (2020)
[29] Z. Li, X. Guo, Y. Zhang, G. Liu, S. Zhang, Chem. Res. Chin. Univ. **36**, 1217 (2020)
[30] L.Y. Cui, X.T. Li, R.C. Zeng, S.Q. Li, E.H. Han, L. Song, Front. Mater. Sci. **11**, 284 (2017)
[31] S. Jin, D. Zhang, X. Lu, Y. Zhang, L. Tan, Y. Liu, Q. Wang, J. Mater. Sci. Technol. **47**, 190 (2020)
[32] C. Dou, M. Zhang, D. Ren, H. Ji, Z. Yi, S. Wang, Z. Liu, Q. Wang, Y. Zheng, Z. Zhang, J. Mater. Sci. Technol. **146**, 211 (2023)
[33] W. Hu, W. Huang, Y. Sun, W. Zhang, L. Tan, S. Zhang, G. Ma, D. Zhang, Q. Wang, J. Mater. Res. Technol. **22**, 2627 (2023)

[34] M. Liu, J. Wang, S. Zhu, Y. Zhang, Y. Sun, L. Wang, S. Guan, J. Magnes. Alloy. **8**, 231 (2020)

[35] J. Chen, S. Wei, L. Tan, K. Yang, Mater. Technol. **34**, 592 (2019)

[36] S. Jafari, R.K. Singh Raman, C.H.J. Davies, Eng. Fract. Mech. **137**, 2 (2015)

[37] D. Bian, W. Zhou, Y. Liu, N. Li, Y. Zheng, Z. Sun, Acta Biomater. **41**, 351 (2016)

[38] D. Bian, W. Zhou, J. Deng, Y. Liu, W. Li, X. Chu, P. Xiu, H. Cai, Y. Kou, B. Jiang, Y. Zheng, Acta Biomater. **64**, 421 (2017)

[39] J. Chen, L. Tan, I.P. Etim, K. Yang, Mater. Technol. **33**, 659 (2018)

[40] X. Cui, S. Zhang, Z.Y. Wang, C.H. Zhang, C.L. Ni, C.L. Wu, Mater. Sci. Eng. A **845**, 143215 (2022)

[41] M.S. Bhuiyan, Y. Mutoh, T. Murai, S. Iwakami, Int. J. Fatigue **30**, 1756 (2008)

[42] X.N. Gu, W.R. Zhou, Y.F. Zheng, Y. Cheng, S.C. Wei, S.P. Zhong, T.F. Xi, L.J. Chen, Acta Biomater. **6**, 4605 (2010)

[43] N. Wegner, D. Kotzem, Y. Wessarges, N. Emminghaus, C. Hoff, J. Tenkamp, J. Hermsdorf, L. Overmeyer, F. Walther, Materials **12**, 2892 (2019)

[44] J. Hu, Q. Li, H. Gao, Acta Metall. Sin. -Engl. Lett. **34**, 65 (2020)

[45] G. Chen, L.T. Lu, Y. Cui, R.S. Xing, H. Gao, X. Chen, Int. J. Fatigue **80**, 364 (2015)

[46] X.Z. Shi, Z.Y. Cui, J. Li, B.C. Hu, Y.Q. An, X. Wang, H.Z. Cui, Acta Metall. Sin. -Engl. Lett. **36**, 1421 (2023)

[47] J. Tong, X. Han, S. Wang, X. Jiang, Energy Fuels **25**, 4006 (2011)

[48] D. Bian, X. Chu, J. Xiao, Z. Tong, H. Huang, Q. Jia, J. Liu, W. Li, H. Yu, Y. He, L. Ma, X. Wang, M. Li, T. Yang, W. Huang, C. Zhang, M. Yao, Y. Zhang, Z. Xu, S. Guan, Y. Zheng, Bioact. Mater. **22**, 180 (2023)

[49] M. Bornapour, N. Muja, D. Shum-Tim, M. Cerruti, M. Pekguleryuz, Acta Biomater. **9**, 5319 (2013)

[50] M. Ascencio, M. Pekguleryuz, S. Omanovic, Corros. Sci. **87**, 489 (2014)

[51] H. Pan, K. Pang, F. Cui, F. Ge, C. Man, X. Wang, Z. Cui, Corros. Sci. **157**, 420 (2019)

[52] L. Han, Z. Zhang, J. Dai, X. Li, J. Bai, Z. Huang, C. Guo, F. Xue, C. Chu, J. Magnes. Alloy. **11**, 1043 (2023)

[53] H. Delavar, A.J. Mostahsan, H. Ibrahim, J. Magnes. Alloy. **11**, 1125 (2023)

[54] D. Mei, C. Wang, S.V. Lamaka, M.L. Zheludkevich, J. Magnes. Alloy. **9**, 805 (2021)

[55] H. Azzeddine, A. Hanna, A. Dakhouche, B. Luthringer-Feyerabend, J. Magnes. Alloy. **9**, 581 (2021)

[56] S. Jafari, R.K.S. Raman, C.H.J. Davies, J. Hofstetter, P.J. Uggowitzer, J.F. Löffler, J. Mech. Behav. Biomed. Mater. **65**, 634 (2017)

[57] M. Linderov, E. Vasilev, D. Merson, M. Markushev, A. Vinogradov, Metals **8**, 20 (2017)